Ultrafast Remote Healing of Magneto-Responsive Thermoplastic Elastomer-Based Nanocomposites

Pablo Griffiths, Gildas Coativy, Florent Dalmas, Guillaume Falco, Liuyin Jiang, Ziyin Xiang, Minh-Quyen Le, Benjamin Ducharne, Damien Le Roy, Françoise Méchin, et al.

Ultrafast Remote Healing of Magneto-Responsive Thermoplastic Elastomer Based Nanocomposites

*Pablo Griffiths,[1,2] Gildas Coativy,[2] Florent Dalmas,[1] Guillaume Falco,[1] Liuyin Jiang,[1,3] Ziyin Xiang,[2] Minh-Quyen Le,[2] Benjamin Ducharne,[2,4] Damien Le Roy,[5] Françoise Méchin,[3] Julien Bernard,[3] Sylvain Meille,[1] and Guilhem P. Baeza[1,]**

[1] Univ Lyon, INSA-Lyon, CNRS, MATEIS, UMR 5510, F-69621 Villeurbanne, France

[2] Univ Lyon, INSA-Lyon, LGEF, EA682, F-69621 Villeurbanne, France

[3] Univ Lyon, INSA Lyon, CNRS, IMP, UMR 5223, F– 69621 Villeurbanne, France

[4] ELyTMaX UMI 3757, CNRS – Université de Lyon – Tohoku University, International Joint Unit, Tohoku University, Sendai, Japan

[5] Univ Lyon, Université Claude Bernard Lyon 1, CNRS, Institut Lumière Matière, UMR 5306, F-69622 Lyon, France

KEYWORDS:

induction heating, stimulus healing, nanocomposites, additive manufacturing, thermoplastic elastomers

ABSTRACT :

We describe herein, a general, efficient and scalable process to design magneto-responsive thermoplastic elastomer-based (nano)composites that can be repeatedly healed in a few tens of seconds by triggering polymer melting upon exposure to a high frequency magnetic field. Three series of composites loaded with 1-15 vol.% of Fe_3O_4 nanoparticles, Fe nanoparticles or Fe microparticles were produced and characterized in depth with the aim to identify the physical properties required for two applications: 1. Materials healing, that we evaluate through rewelding of pre-cut samples and subsequent tensile tests, and 2. Surface smoothening of 3D-printed objects, serving to remove superficial defects and improve their appearance. The optimal formulation consisting of a composite reinforced with 5 vol.% of Fe nanoparticles ensures a high ability to heat while keeping a low viscosity in the molten state being ideal for polymer processing.

1. INTRODUCTION

Recent societal trends oriented towards the reuse of technological goods have emerged as the antithesis of the built-in obsolescence philosophy. The development of such sustainable approaches is however not an easy task, most often burdened by a limited number of effective repairing and recycling steps of the materials. A typical example is that of filled elastomers, solicited in a cyclic manner over long periods until their inevitable disintegration. This is the case for tires, shoe soles, seals and wire sheaths that generate a massive pollution on land[1-2] and in the oceans.[1]

Yet, a technological gap exists to design repairable and recyclable elastomers. Indeed, although the vulcanization process provides rubber-based materials with unrivalled mechanical properties, the presence of chemical crosslinks prevents their healing and any possible second life. The challenge resides therefore in finding an alternative satisfying highly demanding requirements in terms of modulus, toughness, wear resistance, chemical stability, and cost. Self-healing rubbers based on supramolecular polymer networks gave reason for hope which unfortunately failed to materialize due to their limits in terms of mechanics, chemical endurance (*e.g.*, sensitivity to humidity[3]) and scalability at the industrial level.

A viable solution resides in thermoplastic elastomers (TPE, or TPU standing for thermoplastic polyurethanes) which represent a credible alternative for the production of both rubber-based mass goods and specialty polymers. TPEs are often made of crystallizable multiblock copolymers which form biphasic materials at room temperature. While assemblies of hard segments, playing the role of physical cross-links, confer the rubber its elasticity, the soft phase ensures its flexibility.[4-6] Above their melting temperature, hard-domains dissociate, resulting in chains diffusion and

macroscopic solid-to-liquid transition. On the other hand, when cooled down at service temperature, hard-segments gather back from the liquid state providing solid-like properties to the material. This dual behavior considerably eases the processing of TPEs, enabling reuse, repair and recycling, conversely to vulcanized rubbers.

The pioneering work of Corten and Urban[7] showed the possibility to repair a polymer-based responsive composite through the use of an oscillating magnetic field. However, this study was restricted to a low-T_g (costly) fluorinated terpolymer. Alternatively, Ramanujan et al. developed promising healable rubbers based on copolymers (either polyethylene-vinyl acetate or acrylonitrile butadiene)[8-9] but the lack of systematic physical characterization inhibits the adaptation of the concept to more conventional, *i.e.*, industry-oriented, chemistries. Alternatively, several research groups attempted to control the solid-to-liquid transition in model supramolecular networks through induction heating.[10-12] In these examples, ionic aggregates, terpyridine (TPy) and ureidopyrimidinone (UPy) moieties were respectively used, without providing strong mechanical properties to the materials, which displayed a shear modulus below 1 MPa or a flow regime at room temperature. Importantly, all the above-mentioned materials (excluding ref. 11) were prepared through solvent casting, precluding large scale production. In summary, although magneto-responsive thermoplastic rubbers are henceforth quite popular to serve as actuators,[13-15] it appears that triggering their phase transition in view of a possible healing or post-processing treatment remains a largely uncharted territory, limited to the field of adhesives[16-17] and bio-engineering-oriented hydrogels.[18] Besides, one can also mention the remarkable work of Yang et al. on model magnetic nanocomposites based on (more conventional) polymethyl methacrylate[19] and polypropylene[20] matrixes where microcracks are healed through an optimized induction heating process.

In the present work, we propose to upgrade commercial TPEs towards (nano)composites filled with magnetic particles making them responsive (stimulus-healable), while enhancing their stiffness. We wish to step away from the "self-healing" character that is still of limited interest for structural applications, and to focus on a convenient "healing on-demand" faculty based on induction-heating. The latter feature, based on magnetic hysteresis losses in the case of micro- and nanoparticles,[21] presents several advantages with respect to usual convective heating:

(i) Remote control enables to generate heat through insulating materials (see *e.g.*, the Teflon film we use during healing), being of particular interest for TPE used as adhesives.[16]

(ii) Spatio-selective heating is possible through particles' localization in macro-architectured materials enabling localized phase transitions.

(iii) High tunability of the heating process is achievable because the heat generation does not depend only on the external stimulus but also on the material's properties (*e.g.*, content and nature of particles as well as matrix viscosity).[21]

We first describe in details the structure of three series of magnetic nanocomposites (filled with either Fe or Fe_3O_4 nanoparticles, or Fe microparticles) and their physico-chemical properties, *i.e.*, thermal, rheological and magnetic characteristics, with regard to their composition. Next, we study in a systematic way the heating efficiency displayed by these materials upon exposure to oscillatory magnetic fields and show how the nature and the volume fraction of magnetic particles enable precise tuning of the temperature increase in the composites. With possible applications in mind, we then investigate the solid-state mechanics of pristine and magnetically healed composites to demonstrate that recovery can be achieved within a minute through induction heating. Finally, based on our optimal formulation containing 5 vol.% of Fe nanoparticles, we produce samples through additive manufacturing and use our technology to smoothen their surface.

2. MATERIALS AND METHODS

2.1.Materials

Polymer Matrix: The polymer matrix is a commercial TPU, Desmopan 85085A (Covestro, Germany) with M_w = 120 kg mol^{-1} and molar-mass dispersity = 2. The content in hard-segments (HDI-HDO-HDI) is 28 wt.%. The soft-segments are made of two different motifs (SS1: butanediol polyadipate) and SS2 (polypropylene oxide) respectively representing 50 wt. % and 22 wt.% of the TPU (see SI section 1 for the full NMR characterization of the TPU).

Magnetic Fillers: The three magnetic nanoparticles (powders) were purchased from Nanografi (Turkey). For the sake of simplicity and possible upscaling no surface functionalization was performed. We refer to these particles as Fe_3O_4 (magnetite nanoparticles), Fe-n (iron nanoparticles) and Fe-µ (iron microparticles). Particles sizes are displayed in Table 1.

Table 1: Particles size as provided by the supplier and determined through image analysis from nanocomposites micrographs. $\overline{d_n}$ and $\overline{d_w}$ refer to the average diameters in number and in weight respectively. Corresponding histograms are provided in Figure 2D, 2H and 2L.

	Fe_3O_4	**Fe-n**	**Fe-µ**
Supplier	14-29 nm	90-100 nm	"325 mesh" (< 44 microns)
Image analysis ($\overline{d_n}$, $\overline{d_w}$)	14 nm, 16 nm	74 nm, 101 nm	3 µm, 39 µm

Composites preparation: Appropriate amounts of TPU (12 g) and (nano)particles (from ca. 1 to 15 g) were first hand-mixed at room temperature. This mixture was then poured into a mini-extruder device having a chamber of 15 cm^3, (DSM Xplore, NL) equipped with two vertical co-rotative screws in a stepwise manner. The extruder chamber was pre-heated at 175 °C ensuring the quick melting of the polymer. The rotor speed was set to 80 rpm and the mixing time to 5 min once the whole sample poured into the extruder. The so-prepared "raw" composites were then hot-pressed at 180 °C for 3 min under 100 bars and subsequently cooled down in air to room temperature in *ca.* 10 min. The films' thickness was either fixed to 0.5 or 1 mm according to the type of characterization. These composites are referred as 1, 5, 10 and 15 vol.% (see SI section 2 for thermogravimetric analysis).

2.2 Methods

Atomic Force Microscopy (AFM): AFM phase micrographs were performed on a Dimension 3100 equipped with a Nanoscope V scanning probe controller (Bruker, USA) using tapping mode. All experiments were performed in air and at room temperature using noncontact tips with frequencies around 330 kHz, a radius of curvature smaller than 7 nm, and a nominal spring constant of 42 N m^{-1} (PPP-NCH from Nanosensor, Switzerland). The neat TPU displayed in Figure 1B was extruded similarly as the composites and subsequently hot-pressed at 160 °C for 3 minutes.

Small Angle X-ray Scattering (SAXS): The SAXS experiment presented in Figure 1C was carried out on a Xeuss 2.0 apparatus (Xenocs, FR) at the Laboratoire Léon Brillouin (LLB, CEA Saclay, France). The instrument uses a microfocused Cu-Kα1 source with a wavelength of 1.54 Å and a Pilatus3 detector (Dectris, Switzerland). The TPU was shaped into 1 mm thick films and the sample-detector distance was set to 2.5 m to achieve a q-range from 0.03 - 2 nm^{-1}. Data were

corrected from the background, transmission and thickness sample to obtain the scattering intensity in absolute units (cm^{-1}). SAXS results measured on Fe_3O_4 and Fe-n based nanocomposites are presented in SI Section 3.

X-ray Diffraction (XRD): XRD measurements were performed at room temperature on a D8 advance apparatus (Bruker, USA) using Cu-Kα1 radiation. Diffraction patterns of our powders were recorded in the 2θ range of 20−90°.

Transmission Electron Microscopy (TEM): For conventional TEM observations, thin sections were prepared by cryo-ultramicrotomy using a Leica Ultracut UCT microtome (Germany) with a diamond knife from DiAtome, United Kingdom. The temperature of the sample and the cutting speed were set to -80 °C and 0.3 mm s^{-1} respectively. Sections of about 90 nm thick were dry-collected and placed on a 400-mesh copper grid. TEM images were acquired using a CM120 Philips transmission electron microscope operating at an accelerating voltage of 120 kV.

Scanning Electron Microscopy (SEM): Powders and composites micrographs were obtained from a VEGA3 apparatus (TESCAN, USA). The acceleration voltage of the electrons was set to 10-20 kV, and the beam intensity "BI" was varied from 3 to 13. Either secondary or backscattered electrons were used (see micrographs). Focused Ion Beam – Scanning Electron Microscope (FIB-SEM) required a two-step milling procedure on the bulk nanocomposite surface, which had previously been metalized with gold. This procedure used high and fine current beams (4 nA and 80 pA respectively) to analyze a polished surface using an in-lens secondary electron (SE) detector.

Differential Scanning Calorimetry (DSC): A Perkin Elmer DSC 8000 was systematically used. Experiments were run under a nitrogen flow of 20 mL min^{-1} at 10 °C min^{-1}. Samples were first

cooled down to -90 °C and heated up to 220 °C (-80 to 200 °C displayed). This cycle was then repeated once, resulting in the measurements displayed in Figure 3A-C (2nd heating segment).

Rheology: Frequency sweep measurements at 180 °C ($100 > \omega > 0.1$ rad s^{-1} and γ = 10-50 % according to the materials) were all performed in a strain-controlled rheometer (ARES 2KFRTN1 from Rheometric Scientific, currently TA, USA) using stainless steel parallel plates of 8 mm diameter (*ca.* 0.8 mm in sample thickness). A nitrogen convection oven allowed maintaining inert atmosphere with a temperature control better than ±1 °C.

Tensile Tests: Uniaxial tensile tests were performed at room temperature on a 1/ME device (MTS, USA) equipped with a 1 kN load cell at a fixed of rate 10 mm min^{-1}. The samples were shaped into dumbbell pieces having working dimensions of 10.0 × 4.0 × 1.0 mm^3. A minimum of three tests was performed for each configuration.

Induction Heating and Thermal Imaging: Induction heating was performed with a master controller v3+ apparatus (CEIA, Italy) connected to a pancake-shaped (flat spiral) inductor made of two concentric turns. A 0.1 mm-thick Teflon composite tape covered the inductor to protect it from material flowing. The frequency of the magnetic field was set to 855 kHz and its maximum amplitude to *ca.* 10 mT corresponding to an intensity of 19 A in the inductor. The alternative current is delivered through electric pulses. The effective irradiation of the samples is referred to as t_{pulse}/t_{period} and ranges from 17% to 100%; t_{pulse} and t_{period} are respectively the duration of the electromagnetic pulse and the time in-between two pulses such as illustrated in Figure 4C. Because of the square decrease of the magnetic field amplitude with the distance, the healing procedure was performed at a coil-sample distance not exceeding 5 mm. Disk-shaped samples (6 mm in diameter and 0.48-0.52 mm thick) were heated and their temperature variations were

recorded with a PI 450 infrared camera (Optris, Germany) equipped with a 13° lens characterized with an optical resolution of 382 × 288 pixels and a measurement rate of 27 Hz. Temperatures reported in this work refer systematically to the maximal temperature recorded by the device. A schematic representation and photographs of the whole dispositive are displayed in Figure 4A-B. Data were processed with the software Optix PIX Connect in the 20-250 °C temperature range. The healing of dumbbell specimens used for tensile test experiments consisted of cutting samples in two identical pieces and placing them in a silicone mold of corresponding dimensions equipped with an anti-adhesive bottom part. After a minute of induction heating such as illustrated in Figure 8C, the healed specimen was extracted from the mold and measured again (see mechanical tests in Figure 8A).

X-ray microtomography: Tomography imaging was performed on a Phoenix v|tome|x (GE Sensing & Inspection Technologies, USA) with a PaxScan digital X-ray image detector (Varian, USA) at room temperature (ca. 25 °C). We used 80 kV and 180 µA as X-ray parameters, placing the sample vertically at an optimal distance for 3-4 µm for voxel size. 3D reconstructed structures revealing the presence of pores in non-dried healed samples loaded with 5 vol.% in Fe-n particles are available as Supporting Materials. Analogous videos highlighting the good distribution of particles are also provided.

Additive manufacturing: Fused filament fabrication of dumbbell-shaped samples and pyramids was performed on a T333 device from Tobeca (France). The machine was equipped with a pellet's extruder MPE (Tobeca, France) avoiding the additional production of filament. The tests were limited to the case of our optimal formulation consisting of a Desmopan matrix reinforced with 5 vol.% of Fe-n particles. The temperature of the nozzle and the printing stage were set to 210 °C and 50 °C respectively. The printing rate was set to 50 mm s^{-1}.

3. RESULTS AND DISCUSSION

3.1 Formulation and Structure of the Nanocomposites

Nanocomposites were routinely prepared through extrusion from a commercial TPU and magnetic particles (magnetite, nano-iron and micro-iron) respectively referred to as Fe_3O_4, Fe-n and Fe-µ hereafter. The chemical structure of the TPU is illustrated in Figure 1A emphasizing the alternance of soft- and hard segments (denoted respectively SS and HS). The HS are based on 1,6-hexanediol and 1,6-hexamethylene diisocyanate, well-known for providing highly symmetrical crystalline structure,[22] yet with a reasonable melting temperature (*ca.* 150 °C). As expected for this class of polymers,[23-25] AFM experiments reveal that HS aggregate into long (ca. 100-200 nm) and rather straight ribbon-like crystallites evenly spaced every 11-14 nm (Figure 1B), as confirmed statistically through SAXS ($d^* = 2\pi/q^* \approx 13$ nm – Figure 1C). XRD diffractograms emphasizing the purity of the three magnetic powders, and SEM micrographs taken from these "as received" products, are respectively presented in Figure 1D and Figures 1E-G.

After extrusion and subsequent hot pressing, the distribution of fillers within the nanocomposite films is systematically homogeneous at a large lengthscale – see TEM micrographs in Figure 2A, 2E and 2I, representative of the histograms presented in Figures 2D, 2H and 2L. However, a closer look reveals important features. Most Fe_3O_4 elementary particles ($d_{Fe_3O_4}$ = 14-29 nm) are merged into fractal aggregates of ca. 100 nm of diameter (Figure 2B-C), possibly gathering into branches, reminiscent of the morphology of widely used fumed silica.[26] Then, larger spherical Fe-n particles (d_{Fe-n} = 90-100 nm) aggregate into a relatively wide range of objects containing several tens of nanoparticles (Figure 2F-G). For both types of nanoparticles, we refer the reader to SAXS patterns provided in SI section 3 where the high polydispersity limits the quantitative analysis. Finally, Fe-

µ particles appear to be even more polydisperse in size and shape. They contain a great number of micro-particles and a few much larger ones. In addition, needle-like particles, with a typical length of 300 nm and a diameter of 50 nm are observed in Figure 2J-K.

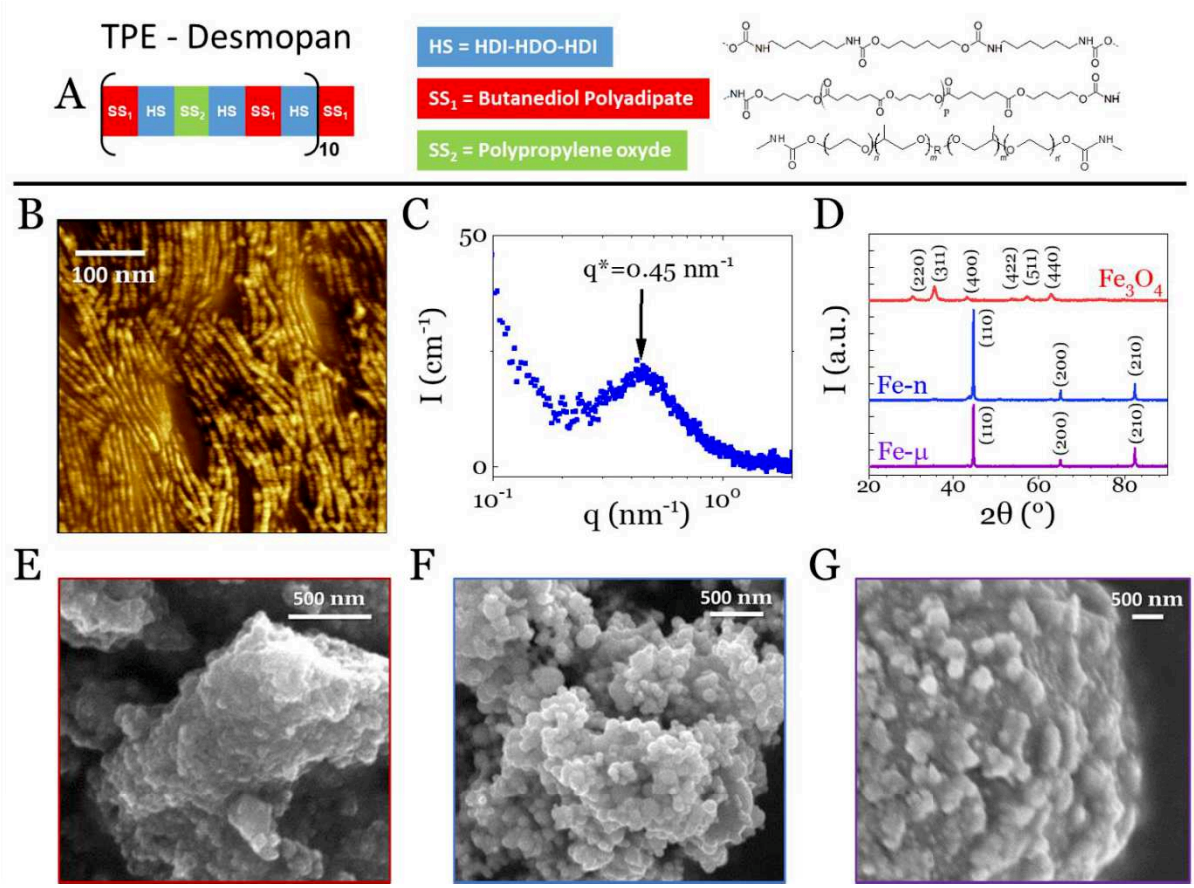

Figure 1. A) Schematic representation of the TPU architecture and corresponding topological formulae of each type of segment. B) AFM micrograph of a hot-pressed sample of Desmopan 85085A. C) SAXS pattern of the Desmopan emphasizing the inter-ribbon distance observed in B. D) XRD patterns of the three magnetic powders. E-G) SEM micrographs of Fe_3O_4, Fe-n and Fe-µ powders.

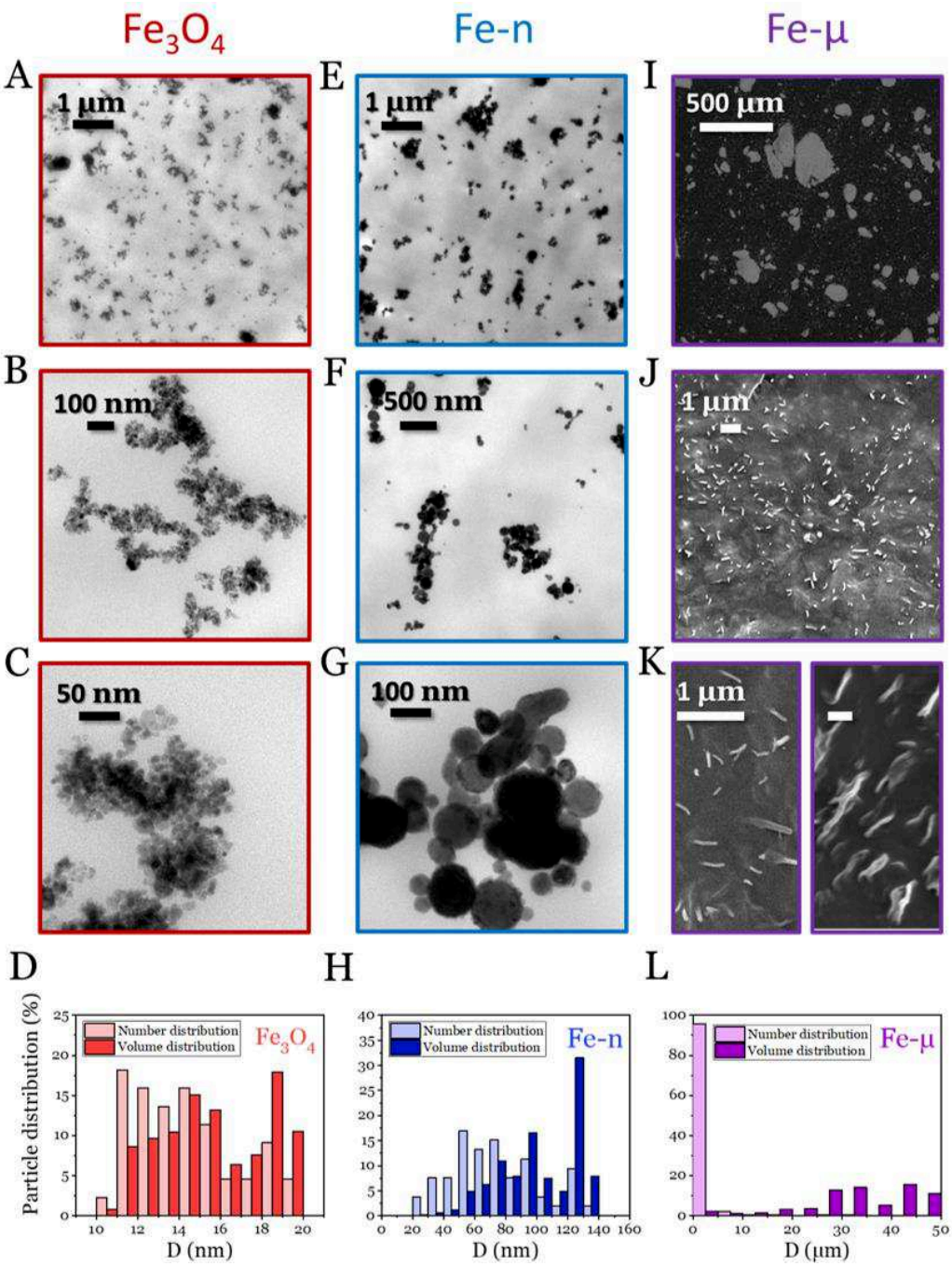

Figure 2. TEM and SEM micrographs of composites containing ca. 5 vol.% in Fe_3O_4 (A-C), Fe-n (E-G) and Fe-μ magnetic particles (I-K). Corresponding number and volume distributions are provided in the histograms (D, H, L); see section 2 for average values. Note that (K) is split into two images representing respectively an isotropic and an aligned arrangement of Fe-μ needles.

3.2 Thermal and Rheological Properties of the Nanocomposites

The choice of a TPU as composite matrix resides in its flexibility at room temperature and its melting point situated below 200 °C. The latter, which depends mainly on the fraction and nature of the HS, ensures a good thermal stability in service while enabling a quick solid-to-liquid transition well before the polymer degradation temperature. However, once filled with nano-objects, TPUs are likely to behave differently, owing to hydrodynamical effects and to interactions between their polar groups (ethers, esters, urethanes) and the surface of the fillers.[27] As a result, physical properties such as glass transition (T_g), melting temperature (T_m) and rheological behavior may be modified.

DSC thermograms of our neat TPU and the three series of composites are presented in Figure 3A-C showing that soft domains exhibit a glass transition at -55 °C regardless of the nature and content in magnetic fillers. A first endothermic peak is observed from 0 to 50 °C corresponding to the melting of SS crystallites made of butanediol polyadipate segments (PABD). The corresponding fraction of crystalline SS is $X_c^{SS} \approx 10$ wt.% in the neat TPU (see details in SI section 1). While Fe_3O_4 and Fe-µ fillers do not show any particular effect on the SS melting, indicating limited interactions between the polymer and the nanoparticles, the situation is different with Fe-n objects whose incorporation progressively results in the disappearance of the SS melting signature. This effect must be understood based on the favorable interactions existing between Fe^{2+} ions at the oxidized Fe-n particles surface and the most polar segments of the TPU (PABD SS and HS) whereas OH group detected on Fe_3O_4 particles seem not to interact favorably with them (see FTIR spectra in SI section 4). More expectedly, the lack of visible interaction between the polymer and the Fe-µ particles undoubtedly stems from their much lower specific surface area. Beyond the impact on the SS crystallites, increasing the content in Fe-n nanoparticles is further

seen to reduce both the melting point and the fraction of crystalline HS, synonymous of a significant alteration of the whole polymer network. All these observations are summarized in Figure 3G, where we represent both the SS and HS melting enthalpy as a function of the filler fraction. Importantly, all the crystalline domains of TPU have completed their melting above 150 °C. The HS crystalline content, which systematically decreases with increasing the filler content, varies in-between $X_c^{HS} \approx 11$ % and 15 % in the Fe_3O_4 and Fe-μ series, while it is slightly lower in the Fe-n one, varying in-between $X_c^{HS} \approx 10$ % and 12.6 %.

While necessary, TPU melting is not a sufficient condition to make the composites flow and promote macroscopic healing or surface smoothening. Indeed, it is well known that the addition of micro- and/or nanoparticles to a polymer melt changes its rheological properties. The latter are mostly dependent on the particles fraction and dispersion as well as their interactions with the polymer chains. Series of frequency sweep measurements, (storage (G') and loss (G'') shear moduli as a function of the pulsation ω), performed on the three types of nanocomposites far above the TPU melting point ($T = 180$ °C) are presented in Figure 3D-F. While in the case of homogeneous liquid-like materials such as molten TPUs, one expects $G' < G''$ with $G' \sim \omega^2$ and $G'' \sim \omega^1$ (Maxwell fluid[28]), adding progressively particles is expected to make them more elastic until reaching a possible viscoelastic solid or "gel" state satisfying $G' > G''$ with both G' and G'' being independent of ω.

This usual trend is visible in both Fe_3O_4 and Fe-n series where the nanocomposite melts see their elasticity growing (or $tan(\delta) = G''/G'$ decreasing) with the particles content until reaching solid-like properties at ca. 15 vol.% ($tan(\delta) < 1$). Nevertheless, we believe that the physical origin of such gelation is different in those two systems. Indeed, Fe_3O_4 particles are much smaller and

organized in a different way with respect to the Fe-n ones. In particular, their higher specific surface and their pre-aggregated morphology enhances their ability to form branches likely to percolate across the TPU. In spite of a lower specific surface area, DSC thermograms clearly underlined the preferential interactions of larger and well-spherical Fe-n particles with the TPU, likely to explain the creation of an elastic network in the composite loaded with 15 vol.% in nanoparticles, being as strong as in the case of its Fe_3O_4 counterpart. In great contrast with Fe_3O_4 and Fe-n series, the addition of Fe-µ particles into the TPU are seen to have a quite limited impact on its rheology that we assign to a much lower specific surface area and no significant interaction with the polymer chains, in good agreement with DSC results reported in Figure 3C. For the sake of clarity, we report in Figure 3H the global evolution of the storage modulus at 10 rad s^{-1} ($G'(\omega_{10})$) for the three series of composites. From the sole rheological point of view (Figure 3D-F), *i.e.*, because they flow on a reasonably short timescale (terminal relaxation time well below 0.01 s resulting in $G'' > G'$), the nanocomposites filled with 5 vol.% in particles appear to be promising candidates for the design of healable materials.

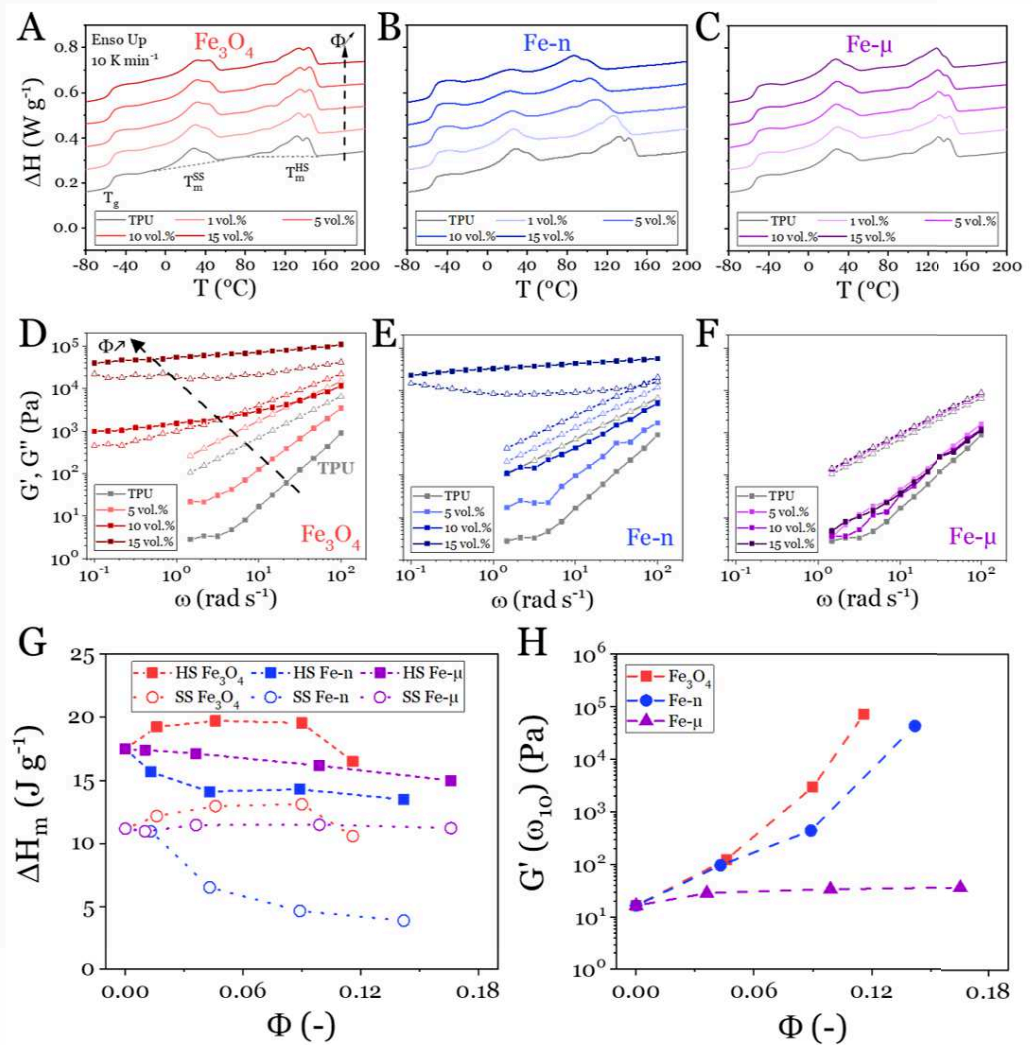

Figure 3. A-C) DSC thermograms measured from the TPU matrix and composites loaded with ca. 1, 5, 10 and 15 vol.% in Fe_3O_4, Fe-n and Fe-μ respectively. The heat flux is normalized by the TPU mass in the sample. Nanocomposites data are shifted for clarity. G) HS and SS melting enthalpy extracted from A-C, dotted lines are guides for the eye. D-F) Rheology frequency sweep measurements performed at 180 °C (1 vol.% data is not shown) for the three composites. Full and open patterns correspond to the shear storage (G') and loss (G'') moduli respectively. H) Shear storage modulus value at 10 rad s^{-1} and 180 °C as a function of the filler volume fraction for the three series of composites – extracted from D-F. Dotted lines are guides for the eye.

3.3 Induction Heating and Thermal Imaging

We next look at the ability to heat of our composites in the presence of an oscillatory magnetic field, targeting 150-200 °C to trigger the TPU melting without degradation. In view of establishing suitable conditions of healing and mechanical recovery, it is mandatory to precisely monitor the temperature evolution during the sample's treatment in order to optimize its flow, *i.e.*, to tune its viscosity so that cracks and micro-defects can be erased without any visible polymer degradation. The induction-heating device used in this work is described in Figure 4A. It includes a high-frequency generator (855 kHz) delivering 19 A in a 2-turns pan-cake coil (Figure 4B). The current is generated in the form of pulses (see Figure 4C). A 3D model of the pancake coil is presented in Figure 4D. The resulting magnetic field profile is established through *Comsol* simulations (see Figure 4E-F), with a maximum magnetic field amplitude of 10-12 mT within the coil and 4-6 mT on top of it, where disk-shaped samples (1 cm diameter) sit during the measurements. The setup is completed by an IR camera enabling an accurate spatio-temporal data acquisition.

The evolution of the temperature as a function of oscillatory magnetic field exposition time is given in Figure 5A-C for the three series of nanocomposites. The Fe_3O_4 series appears to be the simplest to rationalize since it seems to follow the case in which particles dissipate a constant amount of heat in their surrounding medium regardless of the experimental time and temperature. This well-established situation results in an increase of the temperature of the material with a continuously decreasing rate dT/dt until reaching a permanent regime. This profile, fitted with Equation 1, being the 0-dimension solution of the heat equation for a constant energy flux, indicates that a single heating mechanism, assigned to the hysteresis losses occurring in magnetic particles is involved. We refer the reader to SI section 5 for electric and magnetic characterizations of the composites and SI section 6 for more information on the heating mechanisms. In Equation

1, T_0, ΔT and τ stand respectively for the room temperature (≈ 22 °C), the amplitude of the heating process (°C) and its characteristic time (s).

$$T(t) = T_0 + \Delta T(1 - e^{-t/\tau}) \quad (1)$$

While a "single heating mechanism" behavior is also observed for Fe-n and Fe-µ composites at 1 vol.%, the temperature profiles recorded for at higher filler fractions are qualitatively different. In fact, it is clear that a second mechanism is triggered in both series when the materials temperature approaches the TPU melting point at ca. 150 °C. This additional heat dissipation, stems from the dramatic fall of viscosity at the TPU melting point favoring the rotation of nanoparticles (see section 3.4). This motion is not spontaneous as for Brownian relaxation,[29-30] ($\tau_B \gg 1/2\pi f$ – see SI section 6) but results from the applied magnetic field generating a torque in the particles that leads to high-frequency friction with the surrounding polymer and extra-heat dissipation.[31-33] In analogy with Fe_3O_4 data, Fe-n and Fe-µ results were fitted with the Equation 2A-B below

$$T(t < t_m) = T_0 + \Delta T_1(1 - e^{-t/\tau_1}) \quad (2A)$$

$$T(t > t_m) = T_0 + \Delta T_1\left(1 - e^{-t/\tau_1}\right) + \Delta T_2(1 - e^{-(t-t_m)/\tau_2}) \quad (2B)$$

where t_m is the time at which melting happens.

Coming back to the case of Fe_3O_4, no extra heating contribution is seen in the 10 and 15 vol.% composites in spite of $T > T_m$. This result is understood based on both rheological and structural information. First, Fe_3O_4 nanobeads are much aggregated so that, free rotation is hindered when the magnetic field is flipped. Second, heating temperatures above T_m can only be reached above 10 vol.% in particles, corresponding to the apparition of a G' elastic plateau at low frequency

(Figure 3D), indicating limited motion of beads. However, it seems that increasing the pulse duration of the magnetic field allows the melting of the TPU from 5 vol.% in Fe_3O_4, where gelation is not reached yet, allowing motion of least aggregated nanoparticles to generate a slight extra-heating (see Figure 5D).

For the sake of comparison, we collected in Figure 5E all the specific absorption rates (SAR) in W g^{-1} for $t_{pulse}/t_{period} = 17\%$, calculated from:

$$SAR = \frac{C_p}{x_p}\frac{dT}{dt}\bigg|_{t\to 0} \quad (3)$$

where C_p and x_p are the specific heat capacity and mass fraction of fillers. While the SAR order of magnitude is similar for the three series of composites (30-80 W g^{-1}), Fe-n particles appear to be more efficient than Fe_3O_4 and Fe-µ ones in terms of heat generation, which is explained through a higher value of magnetic saturation resulting in a broader $M(H)$ hysteresis loop at high frequency.[34] It is further noteworthy that SAR values remain almost constant with increasing Φ regardless of the particles nature, indicating a limited impact of dipolar interactions.[21,35-37] This is corroborated in Fe_3O_4 and Fe-n series by SAXS diffractograms showing no further aggregation of the particles with increasing Φ (SI section 3).

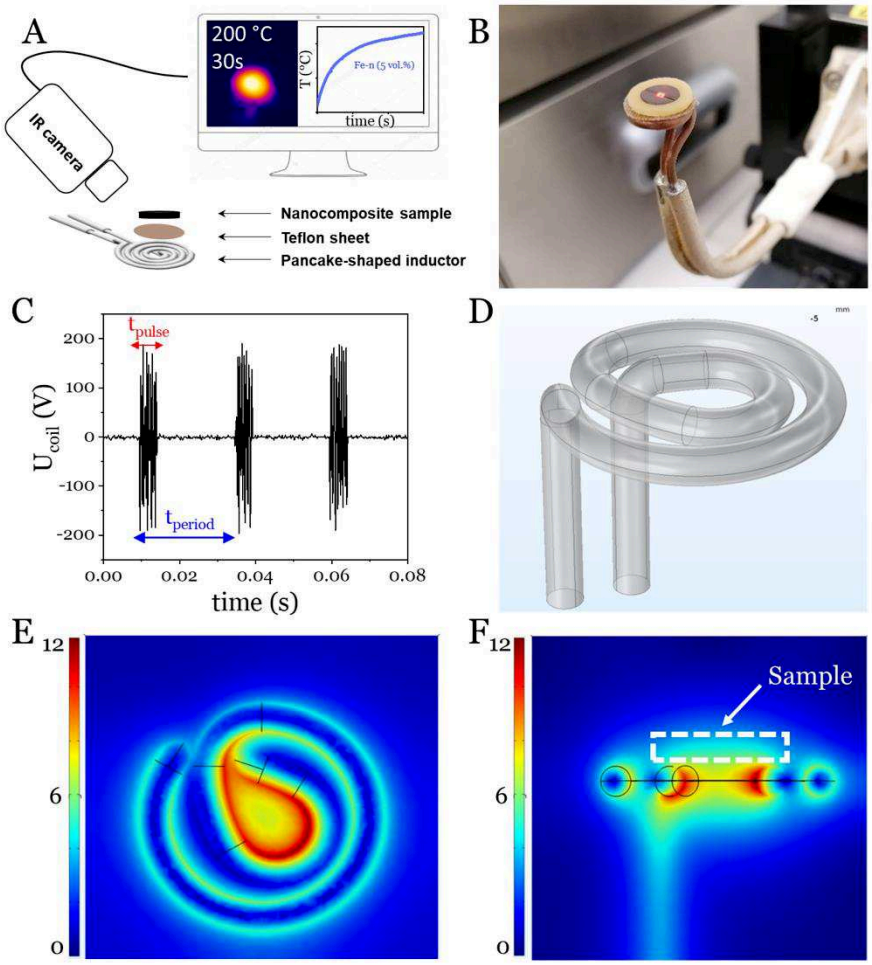

Figure 4. A) Schematic representation of the induction heating setup. B) Photograph of the heating stage made of the pancake-shaped coil, a silicone mold and the sample. The shiny red dot comes from a pyrometer. C) Oscillogram of the voltage applied to the coil during the healing procedure. (t_{pulse}/t_{period} = 17%) D) 3D model of the pancake coil. E) Comsol simulation of the magnetic field generated in the surroundings of the pancake coil during the induction heating process evidencing that its amplitude within the sample does not exceed *ca.* 6 mT. (top view). F) Analogous figure in side view.

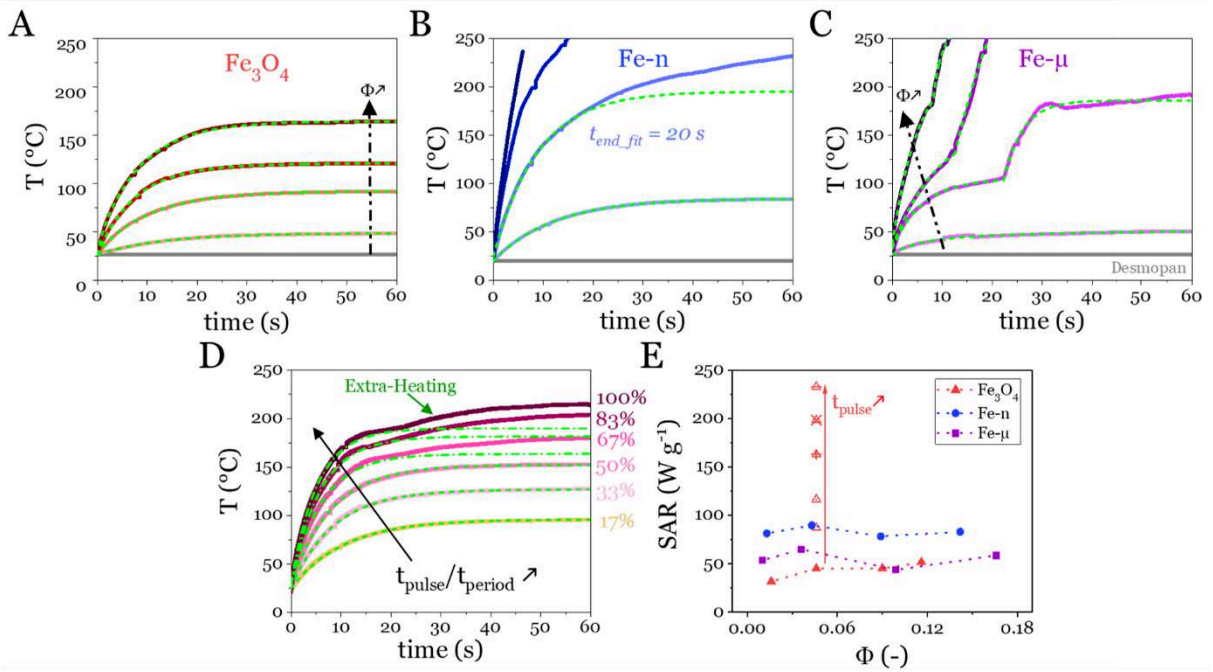

Figure 5. A-C) Temperature profiles as a function of time during induction heating for the three series of composites loaded with ca. 1, 5, 10 and 15 vol.% in Fe_3O_4, Fe-n and Fe-μ respectively (color), the grey line stands for the neat TPU. t_{pulse}/t_{period} was fixed to 17%. Dashed lines are fitted to the Fe_3O_4 and Fe-n (short time) data with Equation 1, and to Fe-μ data with Equation 2. D) Temperature profile of a composite loaded with ca. 5 vol.% in Fe_3O_4 for growing magnetic pulse times. The slight extra-heating indicates possible motion of nanoparticles. E) SAR as a function of the filler volume fraction for the whole set of composites. Dotted lines are guides for the eye representing the evolution of the first heating process only.

3.4 Evidence for particles reorientation under oscillatory magnetic field

The extra-heat generation detected in Fe-n and Fe-μ composites at the TPU melting (see Figure 5B-C) strongly suggests the possibility for the nanoparticles to move under the application of the magnetic field, acting as an external force. On the contrary, the absence of extra-heating in Fe_3O_4 based composites (Figure 5A), including at $T > T_m$, indicates that the motion of such aggregated particles is unlikely. To verify these hypotheses, we present several micrographs in Figure 6. First, we show that Fe-μ needles can be oriented easily in a composite hot-pressed at 180 °C in presence of a permanent magnet (Figure 6A). Then, we used a dual column FIB-SEM to characterize the cross-section of nanocomposites containing ca. 5 vol.% in either Fe_3O_4 or Fe-n. While, Fe_3O_4 particles do not reveal any alignment after 60 s of induction heating (Figure 6B), the same experiment generates a clear alignment of particles in the case of Fe-n fillers (Figure 6C-D, respectively obtained before and after induction heating). We can thus confirm that the high-frequency magnetic field enables both rotational and translational Fe-n particles diffusion, resulting into the creation of dipolar chains likely to impact the heating efficiency and the mechanics of materials healed several times. This important "durability-oriented" question will be examined in a future work involving X-ray photon correlation spectroscopy and thermal imaging performed in-situ during induction heating.

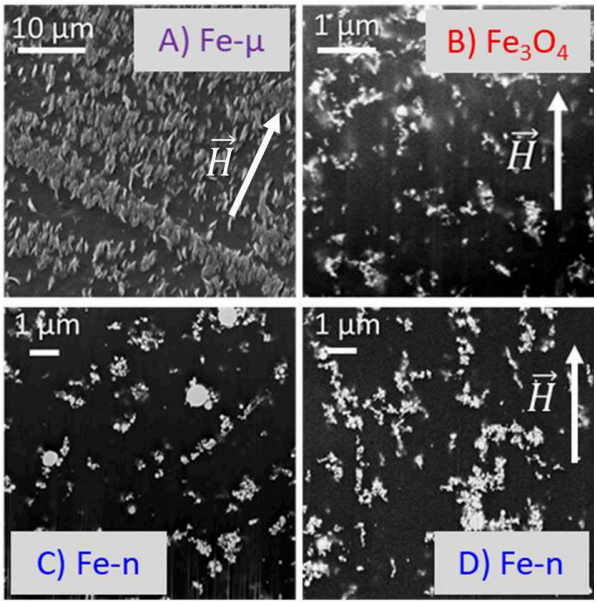

Figure 6. A) SEM micrographs obtained from a composite containing ca. 5 vol.% in Fe-µ particles. Needles are clearly seen to align under a permanent magnetic field. B) FIB-SEM micrographs obtained from a composite containing ca. 5 vol.% in Fe_3O_4 after being healed 60 s, no alignment is observed. C-D) FIB-SEM micrographs from a composite containing ca. 5 vol.% in Fe-n, C) before and D) after healing, where dipolar chains are observed.

3.5 Solid-State Tensile Properties of Nanocomposites

The last requirement in terms of physical properties regards the mechanical performances in service. While adding micro- or nanoparticles to the TPU matrix is expected to enhance its stiffness at low deformation (reinforcement[38]), the behavior at large amplitude may on the other hand, be strongly impacted by the creation of defects favoring crack initiation and propagation. In Figure 7A-C, we present quasi-static tensile tests performed on the three series of nanocomposites revealing these effects. As expected, the drop of toughness is visible in Figure 7D, which gathers the whole data set in terms of energy at failure (W_{break}) versus filler fraction, showing a similar trend regardless of the particle's nature. Besides, the Young's modulus enhancement (Figure 7E) indicates that Fe_3O_4 particles reinforce significantly more the TPU than Fe-n and Fe-µ ones as one may have expected from their higher specific surface and pre-aggregated nature favoring mechanical percolation. Here again, the composites loaded with 5 vol.% appear as a good compromise in terms of solid-state mechanics in spite of their limited reinforcement (ca. 30% stronger than the neat TPU for Fe_3O_4 and Fe-n series).

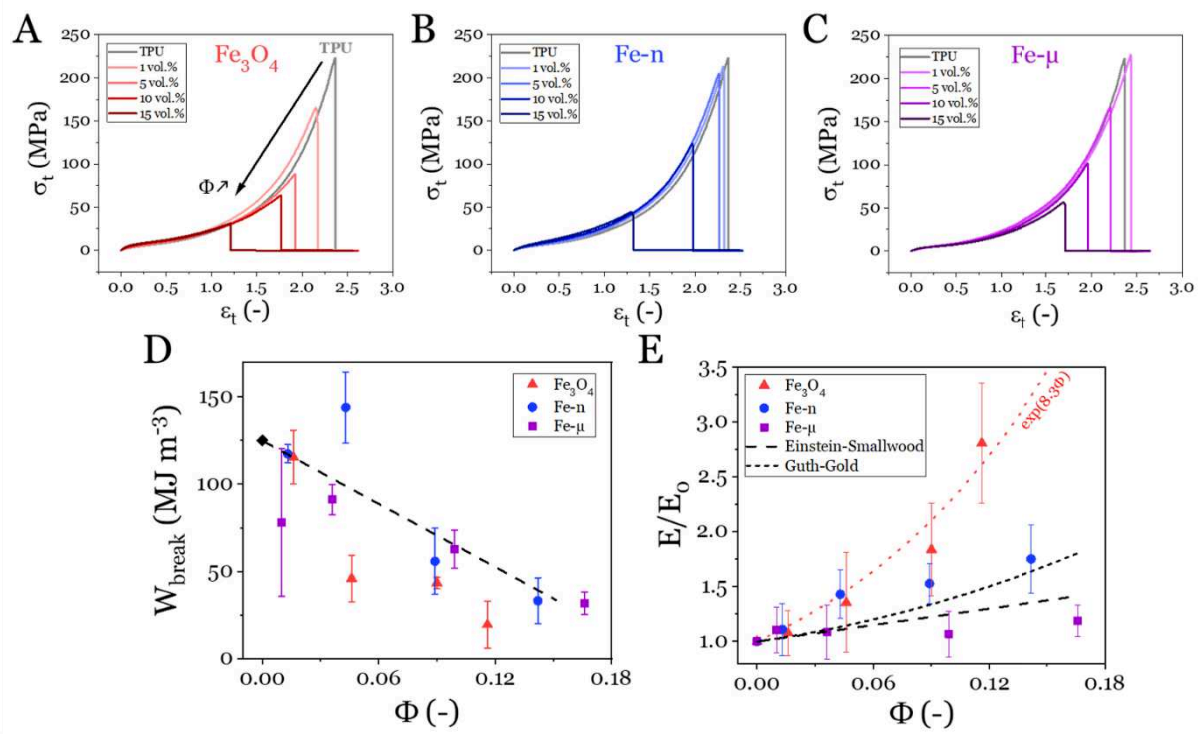

Figure 7. A-C) Tensile tests (true stress vs. true strain) carried out on the TPU matrix and on composites loaded with ca. 1, 5, 10 and 15 vol.% in Fe_3O_4, Fe-n and Fe-μ respectively. D) Energy at failure as a function of the volume fraction in filler for the whole set of composites. The dotted line is a linear guide for the eye. E) Normalized Young's modulus as a function of the filler fraction showing the reinforcement effect. Dashed lines stand for the hydrodynamic models of Einstein-Smallwood $\left(\frac{E}{E_0} = 1 + 2.5\Phi\right)$ and Guth-Gold $\left(\frac{E}{E_0} = 1 + 2.5\Phi + 14.1\,\Phi^2\right)$ giving an idea of the amplitude of the reinforcement.

3.6 Impact of Healing on Tensile Properties and Structure of 5 vol.% Nanocomposites

Following the above characterizations, several healings of composites loaded with ca. 5 vol.% of fillers were performed. These materials are attractive, mainly because they reach a temperature higher than the melting point of the TPU in a few tens of seconds under magnetic stimulus and flow on a short time scale (see Figures 5A-C and 3D-F, respectively). Figure 8A shows tensile-tests experiments where results from *Reshaped* and *Healed I* versions of Fe_3O_4, Fe-n and Fe-µ composites are reported. On one hand, *Reshaped* refers to samples that have been hot-pressed from post-mortem pieces of materials issued from *Original* tests presented in Figure 7. On the other hand, *Healed I* refers to *Reshaped* samples that have been cut into two pieces with a razor blade and subsequently healed locally through thermal induction as shown in Figure 8C-D. For each type of sample, a minimum of three tensile tests were performed (see SI section 7 for all data). The targeted healing temperature was 195 °C ± 15 °C to promote fast chain diffusion without polymer degradation. Accordingly, induction heating was adapted for each type of particles through t_{pulse}/t_{period} (from 17% to 67%) and healing time (45 s or 60 s).

Strikingly, the stress-strain response of the healed materials systematically overlaps with the non-damaged samples up to above 1.2 true strain unit, far above the standard use of common TPU based goods. This is further emphasized in Figure 8B where *Original*, *Reshaped* and *Healed I* samples exhibit identical tensile behaviors, regardless of the particles' nature. Distinctive behaviors are exclusively observed at very high strain where *Healed I* samples systematically show a lower strain at fracture than their *Reshaped* counterparts. This is assigned to a different microstructure around the healed zone caused by the persisting phase separation within the liquid TPU, as observed at low frequency in Figures 3D-F. In fact, this lack of dissociation during healing inhibits the whole memory erasure, limiting the recovery of the TPU structure once cooled down.

In addition, structural reorganization of the particles in Fe-n and Fe-μ composites (Figure 6) are also expected to impact the behavior at large strain.

To track the potential formation of defects upon mending, we further performed X-ray tomography on a 5 vol.% Fe-n composite before and after the induction healing process (see Figure 8E-G and corresponding videos in Supplementary Materials). Although samples looked similar macroscopically, X-ray tomography revealed the presence of large holes in *Healed I* materials that were formed during the healing process owing to evaporation of residual water in the TPU (see Figure 8F). Consistent with our thoughts, no hole was detected in mended composites when the samples were vacuum-dried before healing; Figure 8G and its corresponding video shows complete structural recovery. Note though that such sample treatment is generally not mandatory as similar mechanical recovery was observed in Figure 8A for hole-containing and hole-free composites. This is explained by the large size of the critical defect admissible in relatively soft rubber-based materials.

Beyond this high mechanical recovery, another asset of our procedure is that the composites healing is extremely fast –1 minute or less– making any comparison with self-healing mechanisms irrelevant (see the Graphical Abstract adapted from ref. 39, which further illustrates the high mechanical properties of the so-healed materials). For example, the pioneer work of Cordier *et al.* demonstrated 85% recovery of the tensile properties after 180 minutes.[40]

To illustrate the general character of our approach, we have further proven that the same procedure can be effectively applied for the reparation of any TPE (see SI section 8). We prepared a 5 vol.% Fe-n composite using another TPE made of polybutylene-terephthalate and polytetrahydrofuran with a higher HS melting point (i.e., 180 °C). As expected, an additional

heating contribution coming from particles reorientation was observed above this temperature when induction heating was used. Tensile tests on healed samples confirmed that this material could also be successfully repaired albeit suffering from the same limitations at high strain.

Our methodology is therefore effective regardless of the nature of the magnetic filler and of the TPU and can be optimized based on the properties we identified in this work. For example, it is worth pointing out that Fe_3O_4 and Fe-µ based materials are slightly more fragile (*Original* and *Reshaped*) and less healable (*Healed 1*) than their Fe-n-based counterparts (see Figures 7A-C and 8A). As suggested from DSC thermograms, we believe that lower elongations at break are due to weaker interactions between the polymer chains and the particles.

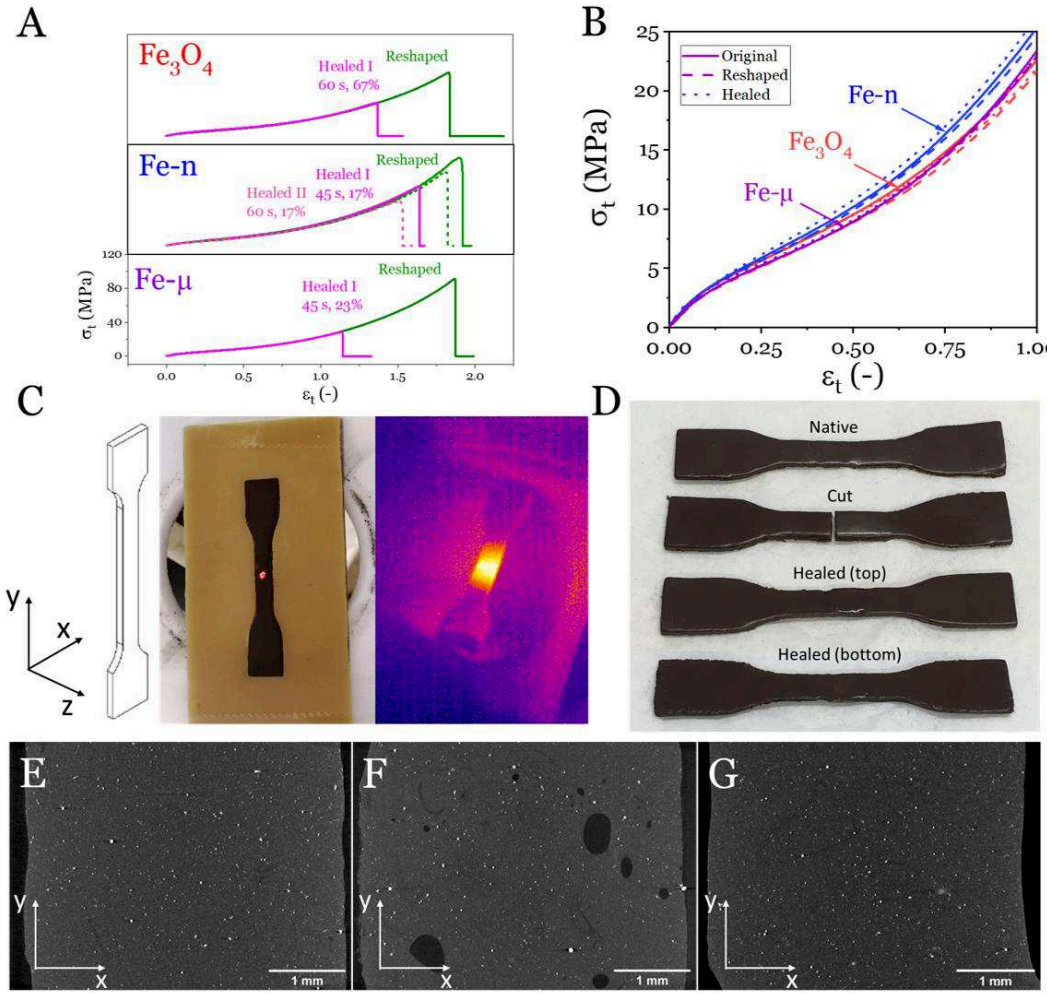

Figure 8. A) Tensile tests performed on nanocomposites loaded with ca. 5 vol.% in Fe_3O_4, Fe-n and Fe-μ. See text for *Original*, *Reshaped*, *Healed I* and *Healed II* mentions. Reported heating duration and t_{pulse}/t_{period} were adapted according to the particle's SAR. B) Zoom-in tensile curves at low and moderate strain amplitudes. C) Photograph of the setup during the healing process. Thermal imaging indicates the zone of the sample affected by induction heating. D) Photograph of a sample at different stages of the healing procedure. E-F-G) Tomography micrographs of *Reshaped*, *Healed I* and *Healed II* composites loaded with 5 vol.% in Fe-n particles, respectively. Corresponding videos and 3D reconstructions are provided as Supplementary Material.

3.7 Induction heating as a post-treatment of 3D printed objects

In this last part, we present some opportunities that offers our technology regarding the post-treatment of objects produced through fused filament deposition, unavoidably presenting topographic defects that are sometimes smoothened by using solvent vapor treatments. Here, the solid-to-liquid phase transition triggered by the magnetic field enables to melt the surface of the so-prepared object, letting the surface tension of the resulting liquid driving the surface quality. The contactless nature, the rapidity, the limited penetration of the magnetic field and the possibility to use co-deposition to tailor the location of the nanoparticles are strong assets in view of a possible upscaling at the industrial level.

To illustrate the potential of this approach, we first manually applied the magnetic field on a face of a truncated pyramid (Figure 9A) made through fused filament deposition of our TPU based composites loaded with 5 vol.% in Fe-n particles. While the surface imperfections related to the manufacturing process are well visible on the left-hand side, a much smoother surface is obtained after only a few seconds of irradiation (right hand-side). Besides, we repeated this procedure in Figure 9B, where we treated a porous dumbbell-shaped sample. Here again, after a few seconds the matter is densified resulting in a much shinier surface, demonstrating the possibility to reach an “injected look” within a short time.

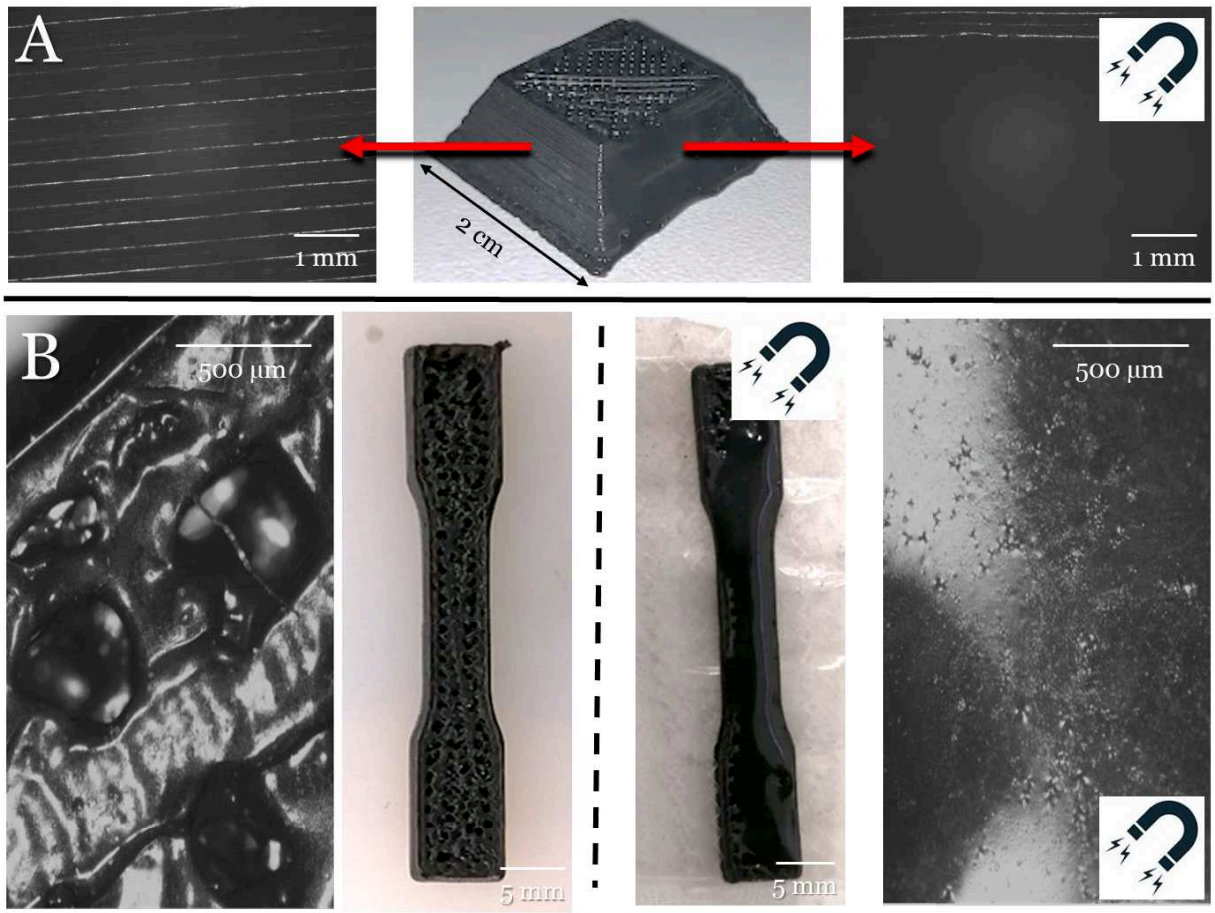

Figure 9. A) Impact of the smoothening procedure on the topography of a truncated pyramid. Optical micrographs of untreated (left) and treated (right) faces. B) Analogous figure for a dumbbell-shaped sample.

4. CONCLUSION

We developed a simple and straightforward approach to produce ultrafast healable and strong rubber-like materials scalable at the industrial level. These materials are based on common components and can be processed using extrusion, injection as well as fused filament fabrication. This strategy can be successfully applied to a range of magnetic fillers with different dimensions and chemistry so that induction heating parameters can be precisely tuned to fit with the material's solid-to-liquid phase transition. The healed materials exhibit a satisfying recovery of the mechanical properties. Also, the only requirement for the polymer matrix lies in a good compromise of viscosity enabling the material to flow through the cut while preventing the deformation of the sample. This offers a vast field of opportunities for TPU and more conventional thermoplastic homopolymers.

ASSOCIATED CONTENT

Supporting Information.

1. Full chemical characterization of the Desmopan 85085A. 2. Thermogravimetric analysis of all the composites. 3.Small angle X-ray scattering performed on the Fe_3O_4 and Fe-n series of composites. 4. Fourier transform infrared spectroscopy of all the powders. 5. Electric and magnetic characterization of the composites. 6. Quantitative rationalization of the heat generation. 7. Complementary tensile tests. 8. Transposition of the healing procedure onto an alternative polymer.

The following files are available free of charge.

X-ray Tomography: Figure8E(Reshaped).mp4, Figure8F(HealedI).mp4, Figure8G(HealedII).mp4

3D-reconstructed animations : 8F_Healed-non-dried, 8G_Healed-dried

AUTHOR INFORMATION

Corresponding Author

*G.P.B.: guilhem.baeza@insa-lyon.fr

Author Contributions

The manuscript was written through contributions of all authors. All authors have given approval to the final version of the manuscript.

Notes

The authors declare no competing financial interest.

ACKNOWLEDGMENT

All the authors thank Vivien Truchot and Laura Courty (IMP, INSA-Lyon) for their help with the samples' preparation and 3D-printing respectively. Eric Maire and Jérôme Adrien (MATEIS, INSA-Lyon) are gratefully acknowledged for their technical support with the tomography investigations. Jacques Jestin (LLB, CEA Saclay) performed the SAXS measurement on the neat TPU. The NMR Polymer Center of the "Institut de Chimie de Lyon" (FR3023) and especially Dr Fernande Da Cruz-Boisson are acknowledged for assistance and access to the NMR facilities. P.G., G.C., F.M., J.B., S. M. and G.P.B. acknowledge the financial support of the Institut Carnot I@L for the funding assigned to the project POMMADE. G.P.B. acknowledges the financial support of IDEX-Lyon and INSA-Lyon through the program ELAN-ERC. All the authors are indebted to the ''Microstructure Technological Center'' (CTμ) of University of Lyon for the access to the transmission electron microscope and the ultramicrotomy device.

REFERENCES

[1] J. Boucher and D. Friot, Primary microplastics in the oceans: a global evaluation of sources, Iucn Gland, Switzerland, 2017.

[2] F. Sommer, V. Dietze, A. Baum, J. Sauer, S. Gilge, C. Maschowski, R. Gieré and others, «Tire abrasion as a major source of microplastics in the environment,» Aerosol and air quality research, vol. 18, p. 2014–2028, 2018. https://doi.org/10.4209/aaqr.2018.03.0099

[3] A. Louhichi, A. R. Jacob, L. Bouteiller and D. Vlassopoulos, «Humidity affects the viscoelastic properties of supramolecular living polymers,» Journal of Rheology, vol. 61, p. 1173–1182, 2017. https://doi.org/10.1122/1.4997600

[4] R. J. Gaymans, «Segmented copolymers with monodisperse crystallizable hard segments: Novel semi-crystalline materials,» Progress in Polymer Science, vol. 36, pp. 713-748, 2011. https://doi.org/10.1016/j.progpolymsci.2010.07.012

[5] J. G. Drobny, Ed., Handbook of Thermoplastic Elastomers, Second Edition ed., Oxford: William Andrew Publishing, 2014.

[6] G. P. Baeza, A.-C. Genix, C. Degrandcourt, L. Petitjean, J. Gummel, M. Couty and J. Oberdisse, «Multiscale Filler Structure in Simplified Industrial Nanocomposite Silica/SBR Systems Studied by SAXS and TEM,» Macromolecules, vol. 46, pp. 317-329, 2013. https://doi.org/10.1021/ma302248p

[7] C. C. Corten and M. W. Urban, «Repairing polymers using oscillating magnetic field,» Advanced materials, vol. 21, p. 5011–5015, 2009. https://doi.org/10.1002/adma.200901940

[8] A. S. Ahmed and R. V. Ramanujan, «Magnetic field triggered multicycle damage sensing and self healing,» Scientific reports, vol. 5, p. 1–10, 2015. https://doi.org/10.1038/srep13773

[9] R. Panigrahi, M. Zarek, V. Sharma, D. Cohn and R. V. Ramanujan, «Bio-Inspired Multiple Cycle Healing and Damage Sensing in Elastomer–Magnet Nanocomposites,» Macromolecular Chemistry and Physics, vol. 220, p. 1900168, 2019. https://doi.org/10.1002/macp.201900168

[10] N. Hohlbein, A. Shaaban and A. M. Schmidt, «Remote-controlled activation of self-healing behavior in magneto-responsive ionomeric composites,» Polymer, vol. 69, p. 301–309, 2015. https://doi.org/10.1016/j.polymer.2015.04.024

[11] G. Falco, P. Griffiths, C. Coutouly, C.-A. Fustin and G. P. Baeza, «Supramolecular Superparamagnetic Nanocomposites Based on a Magnetite-Filled Unentangled Terpyridine-

Functionalized Polymer,» Macromolecules, vol. 53, p. 5361–5370, 2020. https://doi.org/10.1021/acs.macromol.0c00182

[12] E. Ogliani, L. Yu, I. Javakhishvili and A. L. Skov, «A thermo-reversible silicone elastomer with remotely controlled self-healing,» RSC advances, vol. 8, p. 8285–8291, 2018. https://doi.org/10.1039/C7RA13686B

[13] Y. Chen, X. Zhao, Y. Li, Z.-Y. Jin, Y. Yang, M.-B. Yang and B. Yin, «Light-and magnetic-responsive synergy controlled reconfiguration of polymer nanocomposites with shape memory assisted self-healing performance for soft robotics,» Journal of Materials Chemistry C, 2021. https://doi.org/10.1039/D1TC00468A

[14] R. M. Erb, J. J. Martin, R. Soheilian, C. Pan and J. R. Barber, «Actuating soft matter with magnetic torque,» Advanced Functional Materials, vol. 26, p. 3859–3880, 2016. https://doi.org/10.1002/adfm.201504699

[15] H. Deng, K. Sattari, Y. Xie, P. Liao, Z. Yan and J. Lin, «Laser reprogramming magnetic anisotropy in soft composites for reconfigurable 3D shaping,» Nature communications, vol. 11, p. 1–10, 2020. https://doi.org/10.1038/s41467-020-20229-6

[16] D. Bae, M. J. Moon, M. Y. Shon, S. T. Oh, G. N. Kim and D. W. Yun, «Study on the heating behavior of Ni-embedded thermoplastic polyurethane adhesive film via induction heating,» The Journal of Adhesion, vol. 93, p. 964–979, 2017. https://doi.org/10.1080/00218464.2016.1194205

[17] S. Salimi, T. S. Babra, G. S. Dines, S. W. Baskerville, W. Hayes and B. W. Greenland, «Composite polyurethane adhesives that debond-on-demand by hysteresis heating in an oscillating magnetic field,» European Polymer Journal, vol. 121, p. 109264, 2019. https://doi.org/10.1016/j.eurpolymj.2019.109264

[18] S. Nardecchia, A. Jiménez, J. R. Morillas and J. de Vicente, «Synthesis and rheological properties of 3D structured self-healing magnetic hydrogels,» Polymer, vol. 218, p. 123489, 2021. https://doi.org/10.1016/j.polymer.2021.123489

[19] Y. Yang, L. Gao, J. Xie, Y. Zhou, J. Hu, Q. Li and J. He, «Defect-targeted self-healing of multiscale damage in polymers,» Nanoscale, vol. 12, p. 3605–3613, 2020. https://doi.org/10.1039/C9NR09438E

[20] Y. Yang, J. He, Q. Li, L. Gao, J. Hu, R. Zeng, J. Qin, S. X. Wang and Q. Wang, «Self-healing of electrical damage in polymers using superparamagnetic nanoparticles,» Nature nanotechnology, vol. 14, p. 151–155, 2019. https://doi.org/10.1038/s41565-018-0327-4

[21] A. E. Deatsch and B. A. Evans, «Heating efficiency in magnetic nanoparticle hyperthermia,» Journal of Magnetism and Magnetic Materials, vol. 354, p. 163–172, 2014. https://doi.org/10.1016/j.jmmm.2013.11.006

[22] L. Matějka, M. Špírková, J. Dybal, J. Kredatusová, J. Hodan, A. Zhigunov and M. Šlouf, «Structure evolution during order–disorder transitions in aliphatic polycarbonate based polyurethanes. Self-healing polymer,» Chemical Engineering Journal, vol. 357, p. 611–624, 2019. https://doi.org/10.1016/j.cej.2018.09.118

[23] R. M. Versteegen, R. Kleppinger, R. P. Sijbesma and E. W. Meijer, «Properties and morphology of segmented copoly (ether urea) s with uniform hard segments,» Macromolecules, vol. 39, p. 772–783, 2006. https://doi.org/10.1021/ma051874e

[24] M. Nébouy, A. de Almeida, S. Brottet and G. P. Baeza, «Process-oriented structure tuning of PBT/PTHF thermoplastic elastomers,» Macromolecules, vol. 51, p. 6291–6302, 2018. https://doi.org/10.1021/acs.macromol.8b01279

[25] N. J. Sijbrandi, A. J. Kimenai, E. P. C. Mes, R. Broos, G. Bar, M. Rosenthal, Y. Odarchenko, D. A. Ivanov, P. J. Dijkstra and J. Feijen, «Synthesis, morphology, and properties of segmented poly (ether amide) s with uniform oxalamide-based hard segments,» Macromolecules, vol. 45, p. 3948–3961, 2012. https://doi.org/10.1021/ma2022309

[26] B. Benane, G. P. Baeza, B. Chal, L. Roiban, S. Meille, C. Olagnon, B. Yrieix and G. Foray, «Multiscale structure of super insulation nano-fumed silicas studied by SAXS, tomography and porosimetry,» Acta Materialia, vol. 168, p. 401–410, 2019. https://doi.org/10.1016/j.actamat.2019.02.024

[27] E. J. Bailey and K. I. Winey, «Dynamics of Polymer Segments, Polymer Chains, and Nanoparticles in Polymer Nanocomposite Melts: A Review,» Progress in Polymer Science, p. 101242, 2020. https://doi.org/10.1016/j.progpolymsci.2020.101242

[28] M. Rubinstein and R. H. Colby, Éds., Polymer Physics, Oxford University Press, 2003.

[29] T. E. Torres, E. Lima, M. P. Calatayud, B. Sanz, A. Ibarra, R. Fernández-Pacheco, A. Mayoral, C. Marquina, M. R. Ibarra and G. F. Goya, «The relevance of Brownian relaxation as

power absorption mechanism in Magnetic Hyperthermia,» Scientific reports, vol. 9, p. 1–11, 2019. https://doi.org/10.1038/s41598-019-40341-y

[30] E. C. Abenojar, S. Wickramasinghe, J. Bas-Concepcion and A. C. S. Samia, «Structural effects on the magnetic hyperthermia properties of iron oxide nanoparticles,» Progress in Natural Science: Materials International, vol. 26, p. 440–448, 2016. https://doi.org/10.1016/j.pnsc.2016.09.004

[31] R. Hiergeist, W. Andrä, N. Buske, R. Hergt, I. Hilger, U. Richter and W. Kaiser, «Application of magnetite ferrofluids for hyperthermia,» Journal of Magnetism and Magnetic Materials, vol. 201, p. 420–422, 1999. https://doi.org/10.1016/S0304-8853(99)00145-6

[32] T. Bayerl, R. Schledjewski and P. Mitschang, «Induction heating of thermoplastic materials by particulate heating promoters,» Polymers and Polymer Composites, vol. 20, p. 333–342, 2012. https://doi.org/10.1177/096739111202000401

[33] O. Yassine, A. Zaher, E. Q. Li, A. Alfadhel, J. E. Perez, M. Kavaldzhiev, M. F. Contreras, S. T. Thoroddsen, N. M. Khashab and J. Kosel, «Highly efficient thermoresponsive nanocomposite for controlled release applications,» Scientific reports, vol. 6, p. 1–7, 2016. https://doi.org/10.1038/srep28539

[34] J. M. D. Coey, Magnetic materials, Cambridge university press, 2010, p. 374–438.

[35] P. H. Linh, P. V. Thach, N. A. Tuan, N. C. Thuan, D. H. Manh, N. X. Phuc and L. V. Hong, «Magnetic fluid based on Fe3O4 nanoparticles: Preparation and hyperthermia application,» chez J. Phys. Conf. Ser, 2009. https://doi.org/10.1088/1742-6596/187/1/012069

[36] Y. Piñeiro-Redondo, M. Bañobre-López, I. Pardiñas-Blanco, G. Goya, M. A. López-Quintela and J. Rivas, «The influence of colloidal parameters on the specific power absorption of PAA-coated magnetite nanoparticles,» Nanoscale research letters, vol. 6, p. 1–7, 2011. https://doi.org/10.1186/1556-276X-6-383

[37] A. Urtizberea, E. Natividad, A. Arizaga, M. Castro and A. Mediano, «Specific absorption rates and magnetic properties of ferrofluids with interaction effects at low concentrations,» The Journal of Physical Chemistry C, vol. 114, p. 4916–4922, 2010. https://doi.org/10.1021/jp912076f

[38] Y. Song and Q. Zheng, «Concepts and conflicts in nanoparticles reinforcement to polymers beyond hydrodynamics,» Progress in Materials Science, vol. 84, p. 1–58, 2016. https://doi.org/10.1016/j.pmatsci.2016.09.002

[39] A. Pena-Francesch, H. Jung, M. C. Demirel and M. Sitti, «Biosynthetic self-healing materials for soft machines,» Nature Materials, vol. 19, p. 1230–1235, 2020. https://doi.org/10.1038/s41563-020-0736-2

[40] P. Cordier, F. Tournilhac, C. Soulié-Ziakovic and L. Leibler, «Self-healing and thermoreversible rubber from supramolecular assembly,» Nature, vol. 451, p. 977–980, 2008. https://doi.org/10.1038/nature06669

GRAPHICAL ABSTRACT

For Table of Contents use only (ca. 3.5 x 8.3 cm²)